



Kinetics of heterogeneous nucleation in supersaturated vapor: Fundamental limits to neutral particle detection revisited

| | |
|-------------------------------|---|
| Journal: | <i>Aerosol Science & Technology</i> |
| Manuscript ID: | AST-MS-2011-055.R2 |
| Manuscript Type: | Original Manuscript |
| Date Submitted by the Author: | n/a |
| Complete List of Authors: | McGraw, Robert; Brookhaven National Laboratory, Environmental Sciences Department Wang, Jian; Brookhaven National Laboratory, Environmental Sciences Department Kuang, Chongai; Brookhaven National Laboratory, Environmental Sciences Department |
| Keywords: | nucleation kinetics, heterogeneous nucleation, neutral particle detection, mean first passage time, barrier crossing |
| | |

SCHOLARONE™
Manuscripts

1
2
3 **Kinetics of heterogeneous nucleation in supersaturated vapor: Fundamental limits**
4 **to neutral particle detection revisited**
5

6
7 Robert McGraw, Jian Wang, and Chongai Kuang
8

9 Environmental Sciences Department, Atmospheric Sciences Division, Brookhaven
10 National Laboratory, 11973, New York, USA
11

12
13
14 **Abstract**
15

16 We examine the nucleated (with barrier) activation of perfectly wetting (zero
17 contact angle) particles ranging from essentially bulk size down to approximately one
18 nanometer mass diameter. While similar studies trace back to the pioneering work of
19 Fletcher [1958], we present here a novel approach to the analysis based on general area
20 constructions that enable key thermodynamic properties including surface and bulk
21 contributions to nucleation work to be interpreted geometrically with reference to the
22 Kelvin curve. The kinetics of activation is described in more detail in terms of the mean
23 first passage time (MFPT) for barrier crossing. MFPT theory and benchmark calculations
24 are used to develop and test a new approximate but simpler to use analytic expression for
25 barrier crossing rate. The present study is motivated by recent condensation particle
26 counter (CPC) studies that appear to finally establish the long-predicted detection of
27 “sub-Kelvin” particles in the nano-size regime. Corresponding states thermodynamic and
28 kinetic scaling approaches are used to facilitate the correlation and selection of optimal
29 CPC working fluids and operating conditions based on a new metric for heterogeneous
30 nucleation, the signal to noise ratio, and on physical and chemical properties.
31
32
33
34
35
36
37
38
39
40
41
42
43
44
45
46
47
48
49
50

51
52
53
54 **Keywords:** nucleation kinetics, heterogeneous nucleation, barrier crossing, neutral
55
56
57
58
59
60
particle detection, mean first passage time

1. Introduction

Striking advance has been made over the past several years in condensation particle counter (CPC) development, enabling particles in the sub-3 nm diameter range approaching the size of molecular clusters to be routinely detected in the laboratory [Winkler et al. 2008; Iida et al., 2009; Sipila et al., 2009; Vanhanen et al. 2011] and in the atmosphere [Jiang et al., 2011]. This breakthrough in instrumentation calls for a re-examination of the foundations of heterogeneous nucleation theory, still largely based on the capillarity approximation [Fletcher, 1958], wherein even small clusters are modeled as bulk-property liquid drops, and simplified kinetics. Fletcher's theory predicts heterogeneous nucleation, driven by thermal fluctuations, for the activation of very small particles (less than about 6 nm) whereas larger particles undergo a transition to barrierless growth at the Kelvin limit. Activation by nucleation below the Kelvin limit is a key factor in lowering **detectable** size, but only recently has the process been definitively observed [Winkler et al., 2008]. Another important development has been the screening of multiple CPC working fluids for optimal detector performance in the sub-3 nm regime [Magnusson et al., 2003; Iida et al., 2009].

The present study has several objectives beginning with re-examination of the theory. Any improvement over Fletcher's analysis is not easily done. One can contemplate a first-principles molecular simulation, but an accurate prediction of nucleation rate requires more realistic model potentials than are presently available. Molecular dynamics- and Monte Carlo-based simulations of nucleation, **which utilize the model potentials, are particularly useful at establishing trends** – e.g. identifying even small systematic departures from classical nucleation theory – but such simulations are

1
2
3 beyond the scope of the present study. Instead, we continue to rely on the capillarity
4 approximation for estimating the thermodynamic properties needed for the theory while
5 focusing on improving the kinetics. For this, an analysis of the mean first passage times
6 (MFPTs) required for the aggregate of molecular evaporation/condensation growth steps
7 to reach and exceed the size of the critical cluster (consisting of seed particle plus
8 condensate) is presented. Recent results from Wedekind et al. [2007] are extended for
9 this purpose to the kinetics of heterogeneous nucleation. Series expansions for MFPT and
10 nucleation rate are evaluated numerically and used to derive a simple analytic expression
11 for predicting heterogeneous nucleation rate. Comparison with the full MFPT calculation
12 shows the approximate formula to be accurate to within a few percent for nucleation
13 barrier heights in excess of about $5kT$ – a range well covering the region of interest to the
14 present study.
15
16
17
18
19
20
21
22
23
24
25
26
27
28
29
30

31 Although physical and chemical properties are derived from the capillarity
32 approximation, a new approach to the thermodynamic analysis is presented. As
33 described in Sec. 2, the approach is based on graphical constructions derived from the
34 Kelvin curve. There are several reasons for pursuing the new approach: It provides
35 convenient area constructions for homogeneous and heterogeneous nucleation barriers
36 and a graphical interpretation even for key kinetic terms, such as the Zeldovich factor,
37 used in the newly derived rate expression. The method further simplifies the scaling
38 analysis used to correlate working fluid performance in Sec. 5. Finally the graphical
39 approach provides a molecular-based framework that recovers results from classical
40 nucleation theory when the capillarity approximation is used while retaining applicability
41 even in cases where the classical theory fails (Sec. 6).
42
43
44
45
46
47
48
49
50
51
52
53
54
55
56
57
58
59
60

1
2
3 The new results are discussed in the context of early speculations on the application
4 of nucleation and growth as a detection tool for single neutral molecules and clusters
5 [Reiss et al., 1977]. A full analysis of detection capability will require, among other
6 considerations, going beyond Fletcher theory and viewing heterogeneous nucleation as a
7 multi-component molecular interaction process in the nano regime. Here we take
8 preliminary steps in this direction to show that the new formulation provides a molecular
9 level framework, rooted in mass action and detailed balance, which can be exploited to
10 great advantage in attempts to go beyond classical nucleation theory.
11
12
13
14
15
16
17
18
19
20
21

22 While the results reported here were in preparation the authors learned of a
23 similarly motivated study of heterogeneous nucleation, also based on capillary theory and
24 perfect wetting [Fernandez de la Mora, 2011]. Although there are similarities between the
25 two studies, there are notable differences in approach. **Differences** include the
26 introduction here of corresponding states scaling, mean first passage time kinetics, and
27 novel area constructions that provide a basis for handling departure from capillary theory
28 in the form of positive/negative deviations in **equilibrium** vapor pressure from the Kelvin
29 relation.
30
31
32
33
34
35
36
37
38
39
40

41 **2. Thermodynamic area constructions**

42 This section develops several graphical constructions for key thermodynamic
43 properties that include nucleation barrier height, surface work, and barrier shape. The
44 approach derives from the Kelvin relation, which gives the critical size (generally
45 consisting of seed plus condensed fluid) as a function of vapor saturation ratio:
46
47
48
49
50
51
52

$$53 \ln\left(\frac{P_{eq}(g)}{P_{eq}^{\infty}}\right) = \left(\frac{32\pi}{3}\right)^{1/3} \left(\frac{\sigma v_1^{2/3}}{kT}\right) g^{-1/3}. \quad (2.1)$$

54
55
56
57
58
59
60

Here $g = n_{seed} + n$ is the number of condensed solvent molecules, each of molecular volume v_1 , required to fill the total volume, v , consisting of the seed particle volume, $v_{seed} \equiv n_{seed}v_1$, plus condensate, $v_{cond} = nv_1$. Equivalently, g is the number of liquid-phase condensate molecules present in the same-size homogeneous drop, $v = v_{seed} + v_{cond} = gv_1$. Used here as a continuous parameter, $n_{seed} = v_{seed}/v_1$ refers not to the number of molecules actually present in the seed, but is rather a measure of seed volume. $P_{eq}(g)$ is the vapor pressure in (unstable) equilibrium with the drop and P_{eq}^∞ is the bulk equilibrium vapor pressure over a flat surface. The non-dimensional group of physical constants appearing on the right hand of Eq. 2.1, which will henceforth be written as $\Omega/T \equiv \sigma v_1^{2/3}/kT$, is a convenient scaling parameter used extensively in the sequel. Here σ is bulk surface tension, v_1 is derived from the bulk density, and $\Omega = \sigma v_1^{2/3}/k$ has units of temperature.

Barrier profiles for heterogeneous and homogeneous nucleation may be derived using thermodynamic area constructions similar to those introduced recently to analyze the deliquescence and efflorescence of small particles [McGraw and Lewis, 2009]. For vapor pressures given by the Kelvin relation, these relations are of the form:

$$\frac{W(n)}{kT} = \int_0^n \ln \left(\frac{P_{eq}(n')}{P_{ext}} \right) dn' \quad (2.2)$$

where n is the actual (not volume equivalent) number of condensed solvent molecules present in the particle, n' is a dummy integration variable and $W(n)$ is the reversible work required to condense n molecules from the surrounding external vapor at pressure P_{ext} . The homogeneous nucleation barrier profile is recovered for $n_{seed} = 0$, in which case $n = g$. A derivation of Eq. 2.2 that includes its extension to an arbitrary vapor pressure

dependence on particle size is provided in the supplementary material, together with a detailed **derivation** of the various sub-region **areas**, R_i , indicated Fig 1.

Figure 1 illustrates area constructions for both homogeneous and heterogeneous nucleation using water vapor at 200% relative humidity (RH) as an example. For the homogeneous case the reduced barrier height is (supplementary material):

$$\frac{W_{hom}^*}{kT} = R_1 + R_2, \quad (2.3)$$

which follows from Eq. 2.2 for the upper limit of integration set at $n = n^* = g^*$, the intersection of the Kelvin curve (solid curve) and horizontal dashed line. In the heterogeneous case, for seed volume v_{seed} , the integration in Eq. 2.2 is from $n' = 0$ ($g = v_{seed} / v_1$) to n^* ($g = g^*$), yielding the reduced barrier height (supplementary material)

$$\frac{W_{hetero}^*}{kT} = R_1. \quad (2.4)$$

A conceptual advantage of the new approach is that, in principle, it avoids the arbitrary separation into surface and bulk properties inherent in the capillarity drop model. Thus if the true vapor pressure curve $P_1(n)$ were somehow available, e.g. from a molecular simulation of cluster evaporation rate, Eq. 2.2 would remain valid – the only requirements being an ideal vapor mixture (an excellent approximation at near atmospheric pressure conditions) and cluster condensation and evaporation rates that satisfy detailed balance. In absence of a sufficiently accurate molecular-based approach we continue with the capillarity approximation, in which case the barriers from graphical construction reduce exactly to those derived conventionally from classical nucleation theory (supplementary material).

Several well-known, capillarity-based, relations for the barrier height follow easily from the graphical construction when the vapor pressure is given by the Kelvin relation.

Continuing with the homogeneous case we obtain the two equivalent results:

$$\frac{W_{homo}^*}{kT} = \frac{1}{2} g^* \ln \left(\frac{P_{ext}}{P_{eq}^\infty} \right) = \frac{1}{2} (R_3 + R_4) \quad (2.5a)$$

$$\frac{W_{homo}^*}{kT} = \frac{1}{3} \frac{A^* \sigma}{kT} = \frac{1}{3} (R_1 + R_2 + R_3 + R_4). \quad (2.5b)$$

where $A^* \equiv A(g^*)$ is the surface area of the critical cluster (supplementary material).

Equation 2.5a is important to the scaling analysis of Sec. 5. **Unified** full barrier profiles for either heterogeneous or homogeneous ($n_{seed} = 0$) nucleation follow from Eq. 2.2 with limits of integration from n_{seed} to $n_{seed} + n$ for variable n , where n is the number of molecules of liquid condensate:

$$\frac{W(n)}{kT} = R_1(n) = -n \ln \left(\frac{P_{ext}}{P_{eq}^\infty} \right) + (36\pi)^{1/3} \left(\frac{\Omega}{T} \right) [(n_{seed} + n)^{2/3} - n_{seed}^{2/3}], \quad (2.6)$$

in agreement with the classical result. Ω/T is the previously defined physical constant grouping appearing in parenthesis on the right hand side of Eq. 2.1. The function $R_1(n)$ evaluated at the critical size $n = n^*$ equals R_1 . Dividing the first and second terms on the right hand side of Eq. 2.6 by the middle terms from Eqs. 2.5a and 2.5b, respectively, gives the following working-fluid-independent result:

$$\frac{W(n)}{W_{homo}^*} = 3 \left(\frac{n}{g^*} + f \right)^{2/3} - 2 \left(\frac{n}{g^*} + f \right) - (3f^{2/3} - 2f) \quad (2.7)$$

where $f = v_{seed}/(g^* v_1) = n_{seed}/g^*$ is the ratio of seed volume to volume of the critical particle. Equation 2.7 has been written in expanded form, **where $-2f$ and $2f$ are added to the 2nd and 3rd bracketed terms respectively**, to show that at the critical condition,

1
2
3
4
5
6
7
8
9
10
11
12
13
14
15
16
17
18
19
20
21
22
23
24
25
26
27
28
29
30
31
32
33
34
35
36
37
38
39
40
41
42
43
44
45
46
47
48
49
50
51
52
53
54
55
56
57
58
59
60

$W(n^*) = W^*$, where $n^*/g^* + f = 1$ and the sum of the two leading terms on the right-hand side is unity,

$$\frac{W^*}{W_{homo}^*} = \frac{R_1}{R_1 + R_2} = -3f^{2/3} + 2f + 1. \quad (2.8)$$

The first equality follows Equations 2.3 and 2.4; the “hetero” subscript of Equation 2.4 has been dropped noting that homogeneous nucleation is just a special case of the graphical construction with $R_2 = 0$. The homogeneous ($f = 0$) limit of Eq. 2.7 was utilized previously [McGraw, 2001]. The unified result obtained here shows that the barrier profiles for perfect wetting are characterized by a universal one-parameter family of curves independent of the detailed physio-chemical properties of the condensing fluid. These curves are shown for several values of f in Fig. 2.

For use in the following section we require the Zeldovich factor, which is a measure of barrier curvature at the critical size [Abraham, 1974]:

$$Z = \sqrt{\frac{-1}{2\pi} \left[\frac{\partial^2 (W_{homo}^* / kT)}{\partial g^2} \right]_{g^*}} = \sqrt{\frac{-1}{2\pi} \left[\frac{\partial^2 (W_{hetero}^* / kT)}{\partial n^2} \right]_{n^*}} = \sqrt{\frac{-\gamma}{2\pi}}. \quad (2.9)$$

The first equality is the definition of this quantity. The second equality shows that Z has the same value for the homogeneous nucleation and perfect wetting heterogeneous nucleation cases. This follows by inspection of the graphical construction and provides an interpretation for the second partial derivatives as each equal to the slope, γ , of the tangent line to the Kelvin curve at g^* indicated in Fig. 1. Mathematically this result derives from Equation 2.2: taking the first derivative of this equation with respect to n gives $\ln(P_{eq}(n)/P_{ext})$ on the right side, which on differentiation again gives the slope of $\ln P_{eq}(n)$ at n . Equation 2.9 results with $n = n^*$ and $g = g^*$. That the same Zeldovich

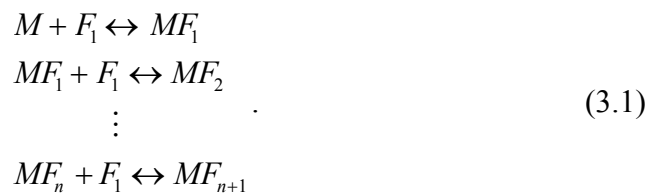
factor applies in the two cases is seen graphically as a simple consequence of the **upper limits of integration** being located at the same Kelvin size. Vehkamäki et al. [2007] provide a convenient formula for evaluating Z for heterogeneous nucleation on spherical particles under more general nonzero contact angle conditions. Using their results we have shown (unpublished) that the same area and slope constructions for W_{hetero}^*/kT and Z , respectively, apply as well in the more general case. Of course $P_{eq}(n)$ depends on contact angle and only (discontinuously) reduces to the Kelvin curve for perfect wetting. Evaluating the slope of the Kelvin curve, **i.e. the derivative of Equation 2.1**, gives:

$$Z = \sqrt{\frac{1}{6\pi} \frac{\ln S_{ext}}{g^*}} = \frac{1}{8\pi} \left(\frac{\Omega}{T}\right)^{-3/2} (\ln S_{ext})^2 \quad (2.10)$$

where in the second equality g^* has been eliminated in favor of $\ln S_{ext} \equiv \ln(P_{ext}/P_{eq}^{\infty})$.

3. Mean first passage time (MFPT) kinetics and activation rate

Consider a collection of condensate free ($n = 0$) seed particles, M , of initial vapor phase concentration $[M]_0 = N(0)$, uniform diameter d_{seed} , and zero contact angle for wetting by the working fluid. The subsequent uptake and exchange of molecules from the working fluid, present in the supersaturated vapor at concentration $[F_1] = n_v$, is described by the following sequence of condensation/evaporation steps:



A similar kinetics applies to homogeneous nucleation on replacement of M by F_1 . Particles sufficiently large (e.g. twice the critical cluster size MF_{n^*}) are assumed far enough into the growth-dominated regime **that they** no longer re-cross the barrier at any

1
2
3 appreciable rate. This is essentially the same argument used to introduce the Szilard
4 absorbing boundary condition in classical nucleation theory [Abraham, 1974] and for the
5 present application justifies the placement of an imaginary model boundary
6 distinguishing “un-activated” from “activated” particles. Because the boundary is in
7 effect absorbing (no-returns) the model activation rate equals the rate of its first crossing,
8 or mean first passage time (MFPT).
9

10
11
12
13
14
15
16
17 Model assumptions: We use an exponential decay kinetics that has previously been
18 applied to activation in supplementary online material by Winkler et al. [2008]:
19

$$20 \frac{dN}{dt} = -J_{hetero} = -J_1 N. \quad (3.2)$$

21
22
23
24
25
26 In the last equality particles are treated as independent to the extent that the steady state
27 nucleation rate, J_{hetero} (number of particles activated per unit volume per second), is
28 proportional to the number concentration of remaining un-activated particles, N :
29
30
31

$$32 J_{hetero} = NJ_1 \quad (3.3)$$

33
34
35
36 where J_1 is the per-particle crossing rate. During a short time interval dt , $J_{hetero} dt$
37 particles per unit volume are lost to activation. Combining these results gives
38
39

$$40 N(t) = N(0)e^{-J_1 t} \quad (3.4)$$

41
42
43 where $N(0)$ is the initial number concentration of seed particles and the exponent gives
44 the probability that any given particle remains un-activated at time t . Several assumptions
45 are implicit in the model that a direct calculation of the MFPT and comparison with
46 measurement can test. First, the assumption of steady state nucleation rate: Conditions
47 under which the quasi equilibration of pre-critical clusters and steady state nucleation are
48 reached on timescales short compared with the decay of N can be seen from a calculation
49 of the MFPT as a function of absorbing boundary location as described in connection
50
51
52
53
54
55
56
57
58
59
60

with Figure 3 below. Second, the exponential decay model requires random rather than deterministic activation – a property that can also be checked through a study of the MFPT. Finally Eq. 3.2 assumes that just one seed particle is present in the critical nucleus. This is easily tested experimentally using the nucleation theorem (Eq. 4.7) below.

Calculation of the mean first passage time: We classify un-activated (activated) particles as those belonging to size class MF_{nmax} and smaller (MF_{nmax+1} and larger) where $nmax = 2n^*$. Interest is primarily in the MFPT to reach MF_{nmax+1} so defined, but a study for variable $nmax$, to show insensitivity to boundary placement at $2n^*$ and verify other assumptions implicit in the exponential model, was also carried out. Let U be the domain of un-activated particles such that $MF_n \in U$ for $0 \leq n \leq nmax$ and let $P_U(t)$ be the probability that a seed that is condensate-free at $t = 0$ remains in the un-activated domain at time t . Then the fraction of particles leaving U at time t is $-dP_U(t)/dt$. By definition, the MFPT is the mean time it takes to leave U , which is [Hänggi, et al., 1990]:

$$\tau \equiv -\int_0^{\infty} t \frac{dP_U}{dt} dt = \int_0^{\infty} P_U(t) dt. \quad (3.5)$$

The last equality follows an integration by parts. Evaluating the last integral using $P_U(t) = N(t)/N(0) = \exp(-J_1 t)$ from Equation 3.4 for the exponential decay model gives $\tau = 1/J_1$, showing that the MFPT equals the reciprocal of the per-particle crossing rate.

Benchmark calculations are based on the following formula for the MFPT [Hänggi et al., 1990; Wedekind et al., 2007]:

$$\tau(nmax) = \sum_{j=0}^{nmax} \left(\frac{e^{W_{hetero}(j)/kT}}{D_j} \sum_{i=0}^j e^{-W_{hetero}(i)/kT} \right). \quad (3.6)$$

The double summation is a discretized version of Eq. 2 of Wedekind et al. [2007]. Dummy indices i and j refer to the number of condensate molecules in the seed-condensate particle (the n in MF_n) and the summation begins with the initial seed, M ($n = 0$). Equation 3.6 describes the case of particles undergoing diffusion-drift along the size coordinate, n , with reflecting and absorbing boundaries located at 0 and $n_{max} + 1$, respectively. D_j is the size-dependent diffusion coefficient along the growth coordinate, which is also equal to the collision rate of vapor molecules with a particle of size $n = j$ ($g = n_{seed} + j$) (McGraw, 2001):

$$D_j = n_v \sqrt{\frac{8\pi kT}{m_v}} r_1^2 (n_{seed} + j)^{2/3} = \frac{P_{ext} A(j)}{\sqrt{2\pi n_v kT}}. \quad (3.7)$$

Here r_1 is the vapor monomer radius corresponding to the molecular volume v_1 , n_v is the vapor number concentration, m_v is vapor molecular mass, and $A(j) = 4\pi r_1^2 (n_{seed} + j)^{2/3}$ is the surface area of the seed-condensate cluster for $n = j$. Direct evaluation of the double summation of Eq. 3.6 provides the benchmark against which a new approximate formulation for J_1 will be tested and used to analyze the scaling properties of heterogeneous particle activation rate in the following section.

4. A simple but accurate expression for mean first passage time and heterogeneous nucleation rate

Figure 3 illustrates a typical distribution of the MFPTs required to exceed any specified (seed plus condensate) particle size as a function of that size or, equivalently, as a function of the upper limit, n_{max} , in the double summation of Eq. 3.6. The steep inflection region centered at the critical size (region II) is indicative of wide separation of time scales between the rapid quasi-equilibration of pre-critical particles (region I) and

the significantly longer times required for barrier crossing and depletion of N , which occur on the order of $\tau = 1/J_1$. The figure also shows the MFPT to be insensitive to n_{max} sufficiently beyond the critical particle size (region III). Henceforth we set $n_{max} = 2n^*$. Starting with Eq. 3.6, a simple but accurate expression can be derived for the mean first passage time and the per-particle heterogeneous nucleation rate. The result, with details of the derivation provided in the supplementary material, is:

$$J_1 = \frac{1}{\tau} \approx \frac{P_{ext} A(j^*)}{\sqrt{2\pi m_v kT}} (1 - e^{-h}) Z e^{-W_{hetero}^* / kT}. \quad (4.1)$$

Multiplication by N gives the total heterogeneous nucleation rate:

$$J_{hetero} \approx N \frac{P_{ext} A(j^*)}{\sqrt{2\pi m_v kT}} (1 - e^{-h}) Z e^{-W_{hetero}^* / kT}. \quad (4.2)$$

The reaction set defined by equation 3.1 describes an associating vapor and a correction for association is included in the rate through the factor $(1 - e^{-h})$ where h is the length of the vertical line segment separating regions R_1 and R_2 in Fig. 1 (see supplementary material). In the limit of large h the distribution of precritical seed-condensate clusters is dominated by the $n = 0$ condensate-free seeds, M and $[M] = N$. For the general case that association is present $[M] = (1 - e^{-h})N$ and Eq. 4.2 becomes:

$$J_{hetero} \approx [M] \frac{P_{ext} A(j^*)}{\sqrt{2\pi m_v kT}} Z e^{-W_{hetero}^* / kT} \quad (4.3)$$

which is proportional to the concentration of the starting species – seeds without condensate. The concentration of condensate-free seeds $[M]$, treated here as just another molecular constituent of the vapor, is reduced below N by the association factor $1 - e^{-h}$, and J_{hetero} is correspondingly reduced. This is an example of the somewhat

counterintuitive effect that association has on increasing the stability of a metastable vapor phase through suppression of the nucleation rate (Katz et al., 1966).

Homogeneous nucleation rate: At high enough saturation ratio, homogeneous nucleation of the vapor itself will compete with heterogeneous nucleation and interfere with particle detection, making the comparison of these two nucleation channels a necessary consideration. The homogeneous nucleation rate is [Abraham, 1974]:

$$J_{homo} = n_v \left(\frac{P_{eq}^\infty}{P_{ext}} \right) \frac{P_{ext} A(g^*)}{\sqrt{2\pi m_v kT}} Z e^{-W_{homo}^* / kT} = n_v^{eq} \frac{P_{ext} A(g^*)}{\sqrt{2\pi m_v kT}} Z e^{-W_{homo}^* / kT} \quad (4.4)$$

As noted previously, Z has the same value here as in the heterogeneous case. The vapor pressure ratio in parenthesis to the right of the first equality supplies the $1/S_{ext}$ correction due to Courtney (1961). It should be noted that Courtney's correction, which derives from the addition of a term $kT \ln(P_{ext}/P_{eq}^\infty)$ to the classical W_{homo} in order to gain consistency with the law of mass action, does not apply to W_{hetero} because the correction cancels on taking free-energy differences relative to M when a seed is present.

Testing the new rate expression: Figures 4 and 5 show the Kelvin curve together with the calculated homogeneous nucleation threshold range from Eq. 4.4 (here shown for rates within ± 2 orders of magnitude of $J_{homo} = 1 \text{ cm}^{-3} \text{ s}^{-1}$) and heterogeneous nucleation threshold range from Eq. 4.1 (rates within ± 2 orders of magnitude of $J_{hetero} = 1 \text{ cm}^{-3} \text{ s}^{-1}$, which numerically equals $J_1(\text{s}^{-1})$ for $N = 1 \text{ cm}^{-3}$). The filled circles are from the full double summation for the MFPT for $\tau = 1 \text{ s}$ (Eq. 3.6 with $n_{max} = 2n^*$) and should be compared with the approximate expression (middle curve) for $J_{hetero} = 1$. Agreement is excellent: to within about 5% in the case of menthol and 2% for water. The larger discrepancy for menthol is probably due to discretization error as the number of

1
2
3 molecules in the critical nucleus is considerably smaller than in the case of water. Barrier
4 heights where the unity nucleation rate thresholds intersect are $18.5kT$ for menthol
5 (Figure 4) and $18.3kT$ for water (Figure 5), i.e. much lower than for homogeneous
6 nucleation where typical barrier heights range between 50 and 70 kT (see below and
7 parameters given in Table 1 for calculation of the heterogeneous nucleation rate). Closer
8 to the region where the seed diameter approaches the Kelvin diameter, e.g. for barrier
9 heights lower than about $5kT$, the approximations used to derive the new analytic
10 expression begin to fail and the full double summation formula for the MFPT should be
11 used instead. The exponential decay model (Eq. 3.4) will also fail in this regime as
12 activation begins to take on less the character of a random barrier crossing process and
13 more one of deterministic growth. According to the $5kT$ criterion the simplified
14 expression for heterogeneous nucleation rate can be used reliably for $f \leq 0.5$ (or
15 d_{seed} / d_{Kelvin} less than about 80%). This is the predominant range of interest anyway as the
16 general goal is to achieve selective detection of the smallest particles, which is favored by
17 being close to the heterogeneous nucleation threshold and well below the Kelvin limit.
18 For $f \leq 0.5$ the association factor is typically between 0.2 and 1 while $1/S_{ext}$ typically
19 exceeds 0.01. In the context of nucleation such corrections are oftentimes regarded as
20 small but here they are needed to achieve the few percent level of accuracy with
21 reference to the MFPT benchmark we have described.

22
23
24
25
26
27
28
29
30
31
32
33
34
35
36
37
38
39
40
41
42
43
44
45
46
47
48
49 Nucleation theorems: Nucleation theorems give the relative sensitivity of nucleation
50 rate to saturation ratio, temperature, or other constraints [Kashchiev, 1982; McGraw and
51 Wu, 2003; Vehkamäki et al., 2007]. The following relations in terms of the log saturation
52
53
54
55
56
57
58
59
60

ratio follow immediately from the area construction (Fig. 1) on application of the fundamental theorem of integral calculus to the areas R_1 and $R_1 + R_2$:

$$\frac{\partial \ln J_{hetero}}{\partial \ln S_{ext}} = \frac{\partial \ln K_{hetero}}{\partial \ln S_{ext}} - \frac{\partial W_{hetero}^* / kT}{\partial \ln S_{ext}} = 1 - \frac{\partial(R_1)}{\partial \ln S_{ext}} = 1 + g^* - n_{seed} = 1 + n^* \quad (4.5)$$

$$\frac{\partial \ln J_{homo}}{\partial \ln S_{ext}} = \frac{\partial \ln K_{homo}}{\partial \ln S_{ext}} - \frac{\partial W_{homo}^* / kT}{\partial \ln S_{ext}} = 1 - \frac{\partial(R_1 + R_2)}{\partial \ln S_{ext}} = 1 + g^*. \quad (4.6)$$

Partial derivatives are taken at constant temperature and K_{hetero} and K_{homo} are the prefactors from Eqs. 4.2 and 4.4, respectively, for the heterogeneous and homogeneous nucleation rate, each of which makes a contribution of unity to the relative sensitivity.

Evaluating instead the relative sensitivity with respect to seed concentration gives:

$$\frac{\partial \ln J_{hetero}}{\partial \ln N} = 1 \quad (4.7)$$

as expected from the one-seed-per-critical-nucleus assumption. More generally, measurement of $\partial \ln J_{hetero} / \partial \ln N$ yields the number of seed particles present in the critical nucleus. Another heterogeneous nucleation theorem that follows immediately from inspection of the area construction gives sensitivity of the log rate to changes in seed particle size, n_{seed} :

$$\frac{\partial \ln J_{hetero}}{\partial n_{seed}} \approx -\frac{\partial R_1}{\partial n_{seed}} = h \quad (h \geq 0). \quad (4.8)$$

The approximate equality neglects a small contribution from the association term in the kinetic prefactor. The requirement that h be non-negative is discussed in Sec. 6.

5. Fundamental limits to neutral particle detection

Maximizing detector sensitivity: Avoiding interference from homogeneous nucleation requires that the homogeneous nucleation rate be less than or comparable to

the activation rate: $J_{homo} / J_{hetero} \leq 1$ or, from Equation 3.3, $J_{homo} / J_1 \leq N(cm^{-3})$. Under typical CPC measuring conditions N is in the 10-1000 cm^{-3} range. Nucleation thresholds are typically sharp, as illustrated for menthol and water in Figures 4 and 5 for $N = 1cm^{-3}$. The figures show threshold bands, where the rates J_{homo} and J_{hetero} take on mid and extreme values of 1, 10^{-2} , and 10^2 , and characteristically small intersection regions where the ratio J_{homo} / J_{hetero} ranges from 10^{-4} to 10^4 . Operating a CPC just below the homogeneous nucleation threshold, $J_{homo} = 1 cm^{-3} s^{-1}$, which condition defines the critical saturation ratio S_{cr} , avoids interference from homogeneous nucleation while maximizing sensitivity for smallest particle detection. The smallest particles will be detected under conditions that are simultaneously close to the homogeneous and heterogeneous nucleation thresholds while preserving the above inequalities. These conditions are used next to establish fundamental size and concentration limits to neutral particle detection.

Signal to noise ratio perspective: Taking nucleation rates from Equations 4.2 and 4.4, the preceding criterion becomes:

$$\frac{J_{homo}}{J_{hetero}} = \frac{n_v^{eq}}{N} \left(\frac{1}{1 - e^{-h}} \right) \frac{A(g^*)}{A(n^*)} e^{-(W_{homo}^* - W_{hetero}^*)/kT} = \frac{n_v^{eq}}{N} \left\{ \left(\frac{1}{1 - e^{-h}} \right) e^{-R_2} \right\}$$

$$\approx \frac{n_v^{eq}}{N} e^{-R_2} = \frac{n_v^{eq}}{N} \exp \left[-\frac{W_{homo}^*}{kT} (3f^{2/3} - 2f) \right] \leq 1. \quad (5.1)$$

The second equality uses the fact that the surface area ratio is unity. As before $f = n_{seed} / g^*$ and R_2 , the area under the Kelvin curve referenced in Fig. 1, has been evaluated in the last equality using Eq. 2.8. In the approximate equality we neglect the inverse association factor, which as noted previously is typically close to unity and much less important to the subsequent discussion than n_v^{eq} , R_2 , or N . The expression to the

1
2
3 right of the approximate equality has an especially transparent interpretation in terms of
4 signal to noise ratio: For steady state homogeneous nucleation the constrained
5
6 equilibrium concentration of clusters of size n_{seed} is given by $n_v^{eq} e^{-R_2}$, where R_2 is the
7
8 reversible work required to assemble a pre-critical cluster of this size from vapor in the
9
10 capillary drop model. (That the concentration of vapor in equilibrium with bulk liquid n_v^{eq}
11
12 appears, rather than the actual supersaturated vapor concentration n_v , follows Courtney
13
14 [1961]). Although these precritical clusters arise from thermal fluctuations in the vapor,
15
16 they have the same probability to subsequently grow to critical size and contribute to
17
18 homogeneous nucleation rate that the permanent perfect wetting seeds have of
19
20 contributing to the heterogeneous nucleation rate. Whenever the two concentrations are
21
22 equal, the homogeneous and heterogeneous nucleation rates will also be the same. The
23
24 expression to the right of the approximate equality is simply this ratio of concentrations:
25
26 fluctuating clusters of seed size (thermal noise) to actual seeds N (signal). Viewed from
27
28 this perspective, the ratio $n_v^{eq} e^{-R_2} / N$, like its equivalent J_{homo} / J_{hetero} , should normally be
29
30 maintained less than unity, and its inverse, the signal to noise ratio (SNR), greater than
31
32 unity in order that the concentration of homogeneously formed clusters not exceed the
33
34 concentration of seeds. (One can conceive of tricks to work with lower SNRs, like
35
36 modulating the seed concentration, but such considerations are beyond the scope of the
37
38 present study). Figure 6 shows curves of constant $SNR = 1$ (equivalently, curves for
39
40 which $N = n_v^{eq} e^{-R_2}$) for *n*-butanol at two different temperatures and three different
41
42 nucleation rates obtained by varying S_{ext} . Detection at smaller size is seen to be favored
43
44 by higher N , lower T , and lower S_{ext} for a relatively lower homogeneous nucleation rate.
45
46
47
48
49
50
51
52
53
54
55
56
57
58
59
60

1
2
3 Scaling and minimum detection size: Because the working fluid enters **primarily**
4 through its equilibrium vapor pressure and non-dimensional *homogeneous* nucleation
5 parameters, corresponding states scaling ideas previously developed to correlate the
6 homogeneous nucleation thresholds of supersaturated vapors [McGraw, 1981;
7 Rasmussen and Babu, 1984; Hale, 1992] can be used here. The power of scaling is
8 illustrated through its application to a selection of four widely different working fluids for
9 which homogeneous nucleation measurements are available (Figure 7 and Table 1).
10 Homogeneous nucleation barrier heights for many substances tend to be in the
11 $50kT - 70kT$ range bounded by the dashed hyperbolic curves [McGraw, 1981], as
12 illustrated for these four fluids in Figure 7. Each of the fluid-characteristic points shown
13 in the figure lies at the intersection of several important curves. **To avoid crowding the**
14 **figure, these are drawn only for nonane to illustrate the method. They include the curve**
15 **of constant homogeneous nucleation barrier height (Equation 2.5a, which if drawn would**
16 **pass through the nonane point and lie within the hyperbolic dashed curves), the Kelvin**
17 **curve, which depends on the scaling parameter Ω/T , and the horizontal and vertical lines**
18 **marking $\ln S_{cr}$ and g^* , respectively. The parameters needed to construct similar sets of**
19 **curves for each of the other working fluids are provided in the table.**

20
21
22 The maximum sensitivity condition for each working fluid lies close to the critical
23 saturation ratio, indicated in Figure 7 for nonane by the horizontal dotted line. The
24 threshold values of first row of Table 1 were obtained from Eq. 4.4 by adjusting S_{ext} to
25 have $J_{homo} = 1$. Thus the minimum **detectable** size lies close to the $\ln(S_{cr})$ line, between 0
26 and g^* , and close to the heterogeneous nucleation threshold. **Its precise location is**
27 **obtained by solving Equation 5.1 (here with seed concentration $N = 1 \text{ cm}^{-3}$) for the**

1
2
3 equality condition $J_{homo} / J_{hetero} = 1$. The result, with $n_{seed}^{min} \equiv f^{min} g^*$, is marked by the caret
4
5
6 in Figure 7 for nonane and provided for the other fluids in row 9 of the Table 1. Near
7
8 constancy of f^{min} (row 7) for the different working fluids suggests its value as an
9
10 important *heterogeneous* nucleation scaling parameter. Using molecular volumes,
11
12 obtained from the bulk liquid density (row 10), to convert n_{seed}^{min} to a spherical mass-
13
14 equivalent volume gives the minimum detectable seed particle diameters shown in the
15
16 last row of the table. The entries for menthol and water match particle diameters at the
17
18 intersection of the threshold rates, $J_{homo} = J_{hetero} = 1$, shown in Figs. 4 and 5, respectively.
19
20
21
22

23 The smallest diameter, at $1.14nm$, is found for water even though its scaling parameters
24
25 are very close to those of *n*-butanol at 300K, which has the second highest minimum
26
27 detection diameter at $1.96nm$. The n_{seed}^{min} values are close for water and *n*-butanol, so the
28
29 difference lays predominately in the smaller molecular volume for water. Comparing
30
31 water and menthol we see that the latter has the highest Ω/T (row 3), which gives it the
32
33 smallest g^* (row 4). Here again water wins out for having the smaller detection diameter
34
35 due to its factor of eight smaller molecular volume.
36
37
38
39

40 The scaling parameter Ω/T contains T implicitly in Ω and explicitly in $1/T$. A
41
42 useful approximate form for the temperature dependence of Ω/T has been obtained by
43
44 Hale [1992] for surface tensions approximated by a linear form, $\sigma = \sigma_0(T_c - T)$, where
45
46 T_c is the critical temperature. Neglecting a small temperature dependence in density gives
47
48 $\Omega/T \approx \Omega_H(T_c/T - 1)$, with $\Omega_H \equiv \sigma_0 v_1^{2/3} / k$. Temperatures dependence is exhibited in
49
50 Fig. 7 for the case of *n*-butanol at 10-degree intervals from 250 to 320K by the triangles
51
52 positioned from left to right, respectively.
53
54
55
56
57
58
59
60

Nucleation and growth as a detection tool: The preceding discussion examined the case that $N \approx 1 \text{ cm}^{-3}$ and applies to the detection of seed particles (or large molecular impurities) of volume $n_{seed}^{min} v_1$ present in the vapor at concentrations of order 1 cm^{-3} . The question naturally arises as to whether or not it is possible to detect still smaller particles and even single neutral molecules this way. According to Eq. 5.1, and Fig. 6, the detection of molecule “impurities” comparable in size to the molecular volume of the working fluid requires their presence at the much higher concentration $N \approx n_v^{eq}$. Intermediate sizes require intermediate seed concentrations N (Fig. 6). Efficiency of particle detection, equal to activation probability within the CPC, is defined as:

$$\varepsilon = 1 - \frac{N(\tau)}{N(0)} = 1 - e^{-J_1 \tau} \quad (5.2)$$

where $N(\tau)$ is the concentration of unactivated particles leaving the CPC after residence time τ . A typical CPC residence time of $\tau = 0.1 \text{ s}$, and $J_1 = 1 \text{ cm}^{-3} \text{ s}^{-1}$, gives $\varepsilon \approx 0.1$, which for this residence time is the detection efficiency at the minimum detectable particle sizes reported in Table 1. Efficiency, being dependent only on the product $J_1 \tau$, is a metric that does not include noise from interfering homogeneous nucleation. On the other hand, from Equation 5.1 $SNR \approx J_{hetero} / J_{homo} = NJ_1 / J_{homo} \approx N\varepsilon / (J_{homo} \tau)$ includes the homogeneous nucleation effect. The last approximation (from Equation 5.2) is useful in the limit of low activation probability. Indeed, ε varies widely along the $SNR = 1$ curves of Figure 6. Thus, having $N = 100 \text{ cm}^{-3}$ gives a noticeably smaller detectable size than having $N = 1$ at the same SNR . These smaller particles will be detectable at the same rate but at only 1% efficiency relative to the (somewhat larger) detectable size limits reported in Table 1 based on having $N = 1 \text{ cm}^{-3}$.

1
2
3 Evidence for the detection of critical nuclei containing just one organic molecule
4 comes from laboratory measurements on the ternary *p*-toluic acid/sulfuric acid/water
5 [Zhang et al., 2004] and *cis*-pinonic acid/sulfuric acid/water [Zhang et al., 2009] systems
6 and their interpretation using the nucleation theorem [McGraw and Zhang, 2008]. In both
7 cases the concentration of the organic acid present in the vapor was of order 10^{10} cm^{-3} -
8 far in excess of unity, and comparable to the sulfuric acid vapor concentration. For a
9 nucleation rate of $10^3 \text{ cm}^{-3} \text{ s}^{-1}$ this implies detection **efficiency** for the organic acid in the
10 10^{-8} range. Noise arises due to binary homogeneous nucleation in the background
11 sulfuric acid/water vapor mixture. Analysis of ternary to binary nucleation rate ratios in
12 the *p*-toluic acid/sulfuric acid/water system [Fig. 4 of McGraw and Zhang, 2008] gives
13 SNRs for detection of *p*-toluic acid in the 5-10 range.
14
15
16
17
18
19
20
21
22
23
24
25
26
27
28

29 In their investigations of nucleation and growth as a detection tool, Reiss et al.
30 [1977] conclude: “it is unlikely, however, that single neutral molecules can be detected
31 [referring to detection using a diffusion cloud chamber], although the possibility remains
32 for detecting individual polymer molecules of a substantial degree of polymerization”.
33 Elsewhere in their paper these authors state, “even though theory shows that one cannot
34 *detect* a single impurity molecule, it shows that there may be cases in which a nucleus
35 contains only a single [such] molecule. But this is not the same as having *every* impurity
36 molecule serve as a nucleus”. Their findings are consistent with the results obtained here.
37 The following section presents a preliminary analysis showing that the graphical method
38 can be used to incorporate departures from the Kelvin relation from interactions at the
39 molecular scale.
40
41
42
43
44
45
46
47
48
49
50
51
52
53
54

55 **6. Incorporating departure from the Kelvin relation**

56
57
58
59
60

1
2
3 An important tool for direct testing of the Kelvin relation for small droplets became
4 available with the ability to measure nucleation rates (as opposed to earlier measurements
5 that yielded only nucleation threshold conditions). Strey et al. [1994] performed such a
6 test using homogeneous nucleation rate measurements in conjunction with the nucleation
7 theorem to give a determination of critical cluster size for *n*-butanol. The Kelvin relation
8 sufficed to predict cluster sizes down to as few as 40 molecules an equivalent radius of
9 curvature of 1 nm. Similar studies for water showed agreement down to about 30
10 molecules or about 0.6 nm radius of curvature [Wölk and Strey, 2001]. One concludes
11 from these studies that even though the Kelvin relation relies on macroscopic surface
12 tension and density to predict the vapor pressures of small drops, it tends to work
13 surprisingly well.
14
15
16
17
18
19
20
21
22
23
24
25
26
27
28

29 A seemingly common case in homogeneous nucleation occurs when the Kelvin
30 relation works well for clusters of critical size but fails for smaller ones. This situation is
31 depicted schematically in Fig. 8 by the dotted vapor pressure curve [$P = P_1(g)$] for the
32 case of attractive interactions that lower the vapor pressures of very small clusters
33 relative to the Kelvin curve. The integrated area between $P_1(g)$ and the dashed line at
34 $\ln S_{ext}$ equals the corrected reduced barrier height for homogeneous nucleation, which in
35 this case is *lower* by κ from the prediction of classical nucleation theory (CNT) based on
36 the Kelvin curve
37
38
39
40
41
42
43
44
45
46
47
48

$$49 \quad \kappa = \int_0^{g^*} \ln [P_{eq}(g) / P_1(g)] dg. \quad (6.1)$$

50
51 In spite of this barrier lowering, g^* and barrier curvature near g^* are the same as in CNT
52 because the location and slope at the crossing point of P_1 and P_{eq} with $\ln S_{ext}$ remain the
53 same. Thus the effect of κ is to cause a uniform vertical shift in the barrier relative to
54
55
56
57
58
59
60

1
2
3 CNT, resulting in either a lower (the case depicted here for $\kappa > 0$) or higher ($\kappa < 0$)
4
5 barrier height: $W_{homo}^* - W_{homo}^*(CNT) = -\kappa kT$. The experimental signature of this effect, in
6
7 accord with the nucleation theorem, is a vertical shift (also by κ) in curves of $\ln J_{homo}$
8
9 versus $\ln S_{ext}$, as is commonly seen in rate measurements [e.g. Strey et al., 1994; Wölk
10
11 and Strey, 2001]. This effect has been studied using molecular-based theory [McGraw
12
13 and Laaksonen, 1996] but the present graphical approach makes it more transparent. For
14
15 the case of *n*-butanol the experimental rate exceeds the CNT prediction by about a factor
16
17 of 10 [Strey et al. 1994] yielding $\kappa \approx 2-3$. For water the observed shifts (and
18
19 corresponding values of κ) are smaller and undergo a change in sign at about 240K
20
21 [Wölk and Strey, 2001].
22
23
24
25
26

27
28 Substrate-working fluid interactions: Molecular scale interactions between a
29
30 particle surface and the working fluid can also result in departure from the Kelvin
31
32 relation. Such interactions are not easily incorporated into macroscopic properties such as
33
34 the contact angles and line tensions used by CNT. Evidence for strong surface effects that
35
36 seem to defy a classical description is seen in recent measurements comparing
37
38 nanometer-sized particles of Ag and NaCl. These substances show very different
39
40 activation efficiency and, in the case of NaCl, unusual temperature dependence
41
42 [Schobesberger et al., 2010]. While not complete without a detailed picture of the
43
44 interactions in question, the graphical method provides a molecular framework for
45
46 generalization of CNT based on deviations in vapor pressure (positive or negative)
47
48 relative to the Kelvin curve. Figure 8 illustrates the case that departures from classical
49
50 homogeneous nucleation theory are due to interactions that take place within clusters of
51
52 the pure working fluid smaller than the seed so that $P_1(g) \approx P_{eq}(g)$ for $g \geq n_{seed}$, but
53
54
55
56
57
58
59
60

interactions between seed and working fluid can still cause departure from the classical heterogeneous nucleation theory for perfect wetting. The effect on vapor pressure is depicted by the dashed curve [$P = P_2(g)$] in Figure 8 for the case of attractive interactions resulting in a vapor pressure lowering near the seed surface. Reduction in h , as suggested in the figure, might possibly be inferred through measurements of the relative sensitivity of heterogeneous nucleation rate to seed size using the nucleation theorem of Eq. 4.8. Note, however, that whenever the vapor pressure at n_{seed} falls below P_{ext} , h becomes negative. Familiar examples occur in Thompson theory, for charged particles, and in Kohler theory for soluble nuclei. In such cases Eq. 4.8 predicts a relative sensitivity of zero as the particle undergoes spontaneous growth until achieving stable equilibrium at P_{ext} . Considering only positive h , the integrated effect of vapor-pressure-lowering interactions is to cause a shift in the heterogeneous nucleation barrier height: $W_{hetero}^* - W_{hetero}^*(CNT) = -\delta kT$, where CNT in parenthesis refers not only to classical nucleation theory but also to perfect wetting. δ is the area indicated in Figure 8:

$$\delta = \int_{g=n_{seed}}^{g^*} \ln[P_1(g)/P_2(g)]dg. \quad (6.2)$$

The κ - and δ -type molecular interactions (Equations 6.1 and 6.2) result in modification of the criterion of Equation 5.1:

$$\frac{J_{homo}}{J_{hetero}} \approx \frac{n_v^{eq}}{N} e^{-R_2} e^{(\kappa-\delta)} \leq 1. \quad (6.3)$$

The methods used to analyze Equation 5.1 are readily carried over to Equation 6.3. Positive values of $\delta - \kappa$ allow for detection of smaller particles. Because measurements suggest that κ is typically quite small (i.e., several kT), almost any kind of molecular bonding between the substrate and working fluid should allow for the detection of

1
2
3 smaller particles than predicted by Equation 5.1. The opposite tendency, requiring a
4 larger particle sizes for the same detection efficiency, follows for repulsive interactions
5
6
7
8 ($\delta < 0$) - including interactions of the type that manifest macroscopically as cases of
9
10 imperfect wetting.

11
12 The results in this section show qualitatively and quantitatively how molecular
13 interactions that lower (elevate) vapor pressure cause enhancement (reduction) of
14 nucleation rate. For the ternary organic acid/sulfuric acid/water systems discussed in Sec.
15 5, recent quantum chemical calculations point to strong organic acid–sulfuric acid
16 hydrogen bonding as responsible for stabilization of the critical complex and
17 enhancement of the nucleation rate seen in laboratory measurements [Zhao et al., 2009].
18
19
20
21
22
23
24
25

26 27 **7. Summary and discussion**

28
29 In this paper we presented theory and a graphical method for analysis of
30 homogeneous and heterogeneous nucleation barriers. The results reproduce classical
31 nucleation theory for the case that the droplet vapor pressure follows the Kelvin relation
32 while allowing interactions at the molecular scale that cause deviations in vapor pressure
33 from the Kelvin result, and from classical nucleation theory, to be formally included.
34 Several nucleation theorems were shown to follow immediately from the graphical
35 method as does the Zeldovich factor, here related to the slope of the Kelvin curve at the
36 critical nucleus size, that appears in expressions for homogeneous and heterogeneous
37 nucleation rate.
38
39
40
41
42
43
44
45
46
47
48
49

50 Calculations based on mean first passage time kinetics were carried out and used as
51 the benchmark to develop and test a new simplified expression for the MFPT and
52 heterogeneous nucleation rate. Including (or not including in the case of heterogeneous
53
54
55
56
57
58
59
60

1
2
3 nucleation) Courtney's $1/S$ correction and allowing for particle-vapor association at pre-
4 critical levels of condensate yielded accuracies **to within** a few percent when compared
5
6 with the MFPT results.
7
8

9
10 Criteria for guiding the selection of working fluids and operating conditions in
11 order to optimize neutral particle detection were derived from a consideration of
12 detection efficiency and a new metric for assessing heterogeneous nucleation – signal to
13 noise ratio. Corresponding states correlations, previously developed in the context of
14 homogeneous nucleation theory, were shown to be applicable to heterogeneous
15 nucleation and used to identify key scaling parameters and obtain results in universal
16 (material independent) form. **Detectability** at minimal seed to molecular volume ratio,
17 $v_{seed}/v_1 = n_{seed}^{min}$, was shown to be favored for larger values of Ω/T , lower vapor
18 concentration, n_v^{eq} , and molecular-level particle-working fluid interactions that lower
19 vapor pressure relative to the Kelvin curve. In the latter case, to the extent such
20 interactions (e.g. hydrogen bonding or antigen-antibody interactions) are favored and
21 characteristically paired, highly selective methods for nanoparticle detection based on
22 nucleation and growth should result. Future research should include extending the
23 graphical method (or equivalent) to multi-component working fluids, more complete
24 development of molecular-based approaches to nucleation theory, and theory and
25 experiment aimed at elucidating temperature dependence.
26
27
28
29
30
31
32
33
34
35
36
37
38
39
40
41
42
43
44
45
46
47

48 **Acknowledgments**

49
50 This research was supported by the Atmospheric System Research (ASR) Program
51 of the U.S. Department of Energy. Special thanks Ernie Lewis for valuable discussions
52
53 **and to an anonymous reviewer for a careful and thoughtful review that greatly helped our**
54
55
56
57
58
59
60

1
2
3 presentation of this work.
4
5

6 **References**
7

- 8 Abraham, F. F. (1974). Homogeneous Nucleation Theory (Academic, New York),
9 Chapt. 5.
10
11 Becker C., and Reiss, H. (1978). Estimation of thermophysical properties of a large polar
12 molecule and application to homogeneous nucleation of *l*-menthol, J. Chem. Phys.
13 68, 3585-3594.
14
15 Courtney, W. G. (1961). Remarks on homogeneous nucleation, J. Chem. Phys. **35**, 2249-
16 2250.
17
18 Fernandez de la Mora, J. (2011). Heterogeneous nucleation with finite activation energy
19 and perfect wetting: Capillary theory versus experiments with nanometer particles,
20 and extrapolations on the smallest detectable nucleus, Aerosol Sci. Technol. **45**,
21 543-554.
22
23 Fletcher, N. H. (1958). Size effect in heterogeneous nucleation, J. Chem. Phys. **29**, 572-
24 576.
25
26 Hale, B. N. (1992). The scaling of nucleation rates, Metallurgical Trans. **23A**, 1863-1868.
27
28 Hänggi, P., Talkner, P., Borkovec, M. (1990). Reaction rate theory: fifty years after
29 Kramers, Rev. Mod. Phys. **62**, 251-341.
30
31 Iida, K., Stolzenburg, M. R., and McMurry, P. H. (2009). Effect of working fluid on sub-
32 2nm particle detection with a laminar flow ultrafine condensation particle counter,
33 Aerosol Sci. Technol. **43**, 81-96.
34
35 Jiang, J., Zhao, J., Chen, M., Eisele, F. L., Scheckman, J., Williams, B. J., Kuang, C., and
36 McMurry, P. H. (2011). First measurements of neutral atmospheric cluster and 1-
37 2nm particle number size distributions during nucleation events, Aerosol Sci.
38 Technol., **45**, ii-v.
39
40 Kashchiev, D. (1982). On the relation between nucleation work, nucleus size, and
41 nucleation rate, J. Chem. Phys. **78**, 5098-5102.
42
43 Katz, J. L., Saltsburg, H., and Reiss, H. (1966). Nucleation in associated vapors, J. Coll.
44 Interface Sci. **21**, 560-568.
45
46 Magnusson, L.-E., Koropchak, J. A., Anisimov, M. P., Poznjakovskiy, V. M., and
47 Fernandez de la Mora, J. (2003). Correlations for vapor nucleating critical embryo
48 parameters, J. Phys. Chem. Ref. Data **32**, 1387- 1410.
49
50
51
52
53
54
55
56
57
58
59
60

- 1
2
3 McGraw, R. (1981). A corresponding states correlation of the homogeneous nucleation
4 thresholds of supercooled vapors, *J. Chem. Phys.* **75**, 5514-5521.
5
6
7 McGraw, R. (2001). Dynamics of barrier crossing in classical nucleation theory, *J. Phys.*
8 *Chem. B* **105**, 11838-11848.
9
10 McGraw, R., and Laaksonen, A. (1996). Scaling properties of the critical nucleus in
11 classical and molecular-based theories of vapor-liquid nucleation, *Phys. Rev. Letts.*
12 **76**, 2754-2757.
13
14
15 McGraw, R., and Wu, D. T. (2003). Kinetic extensions of the nucleation theorem, *J.*
16 *Chem. Phys.* **118**, 9337-9347.
17
18
19 McGraw, R., and Zhang, R. (2008). Multivariate analysis of homogeneous nucleation
20 rate measurements. Nucleation in the p-toluic acid/sulfuric acid/water system, *J.*
21 *Chem. Phys.* **128**, 064508, 1- 9.
22
23
24 McGraw, R., and Lewis, E. R. (2009). Deliquescence and efflorescence of small
25 particles, *J. Chem. Phys.* **131**, 194705, 1-14.
26
27
28 Rasmussen, D. H., and Babu, S. V. (1984). A corresponding states correlation for
29 nucleation from the vapor, *Chem. Phys. Letts.* **108**, 449-451.
30
31
32 Reiss, H., Marvin, D. C., and Heist, R. H. (1977). The use of nucleation and growth as a
33 tool in chemical physics, *J. Coll. Interface Sci.* **38**, 125-141.
34
35
36 Rudek, M. M., Fisk, J. A., Chakarov, V. M., and Katz, J. L. (1996). Condensation of a
37 supersaturated vapor. XII. The homogeneous nucleation of the *n*-alkanes, *J. Chem.*
38 *Phys.* **105**, 4707-4713.
39
40
41 Schobesberger, S., Winkler, P. M., Pinterich, T., Vrtala, A., Kulmala, M., and Wagner, P.
42 E. (2010). Experiments on the temperature dependence of heterogeneous nucleation
43 on nanometer-sized HaCl and Ag particles, *ChemPhysChem* **11**, 3874-3882.
44
45
46 Sipilä, M., et al. (2009). Laboratory verification of PH-CPC's ability to monitor
47 atmospheric sub-3 nm clusters, *Aerosol Sci. Technol.*, **43**, 126-135.
48
49
50 Strey, R., Wagner, P. E., and Viisanen, Y. (1994). The problem of measuring
51 homogeneous nucleation rates and the molecular contents of nuclei: Progress in the
52 form of nucleation pulse measurements, *J. Chem. Phys.* **98**, 7748-7758.
53
54
55 Vanhanen, J., Mikkilä, J., Lehtipalo, K., Sipilä, M., Manninen, H. E., Siivola, E., Petäjä,
56 T., and Kulmala, M. (2011). Particle size magnifier for nano-CN detection, *Aerosol*
57 *Sci. Technol.*, **45**, 533-542.
58
59
60

- 1
2
3 Vehkamäki, H., Määttänen, A., Lauri, A., Napari, I., and Kulmala, M. (2007). Technical
4 Note: The heterogeneous Zeldovich factor, *Atmos. Chem. Phys.* **7**, 309-313.
5
6
7 Vehkamäki, H., Määttänen, A., Lauri, A., Napari, I., and Kulmala, M., Winkler, P.,
8 Vrtala, A., and Wagner, P. E. (2007). Heterogeneous multicomponent nucleation
9 theorems for the analysis of nanoclusters, *J. Chem. Phys.* **126**, 174707, 1-12.
10
11 Wedekind, J., Strey, R., and Reguera, D. (2007). New method to analyze simulations of
12 activated processes, *J. Chem. Phys.* **126**, 134103, 1-12.
13
14
15 Winkler, P. M., Steiner, G., Vrtala, A., Vehkamäki, H., Noppel, M., Lehtinen, K. E. J.,
16 Reischl, G. P., Wagner, P. E., and Kulmala, M. (2008). Heterogeneous nucleation
17 experiments bridging the scale from molecular ion clusters to nanoparticles, *Science*
18 **319**, 1374-1377.
19
20
21 Wölk, J., and Strey, R. (2001). Homogeneous nucleation of H₂O and D₂O in comparison:
22 The isotope effect, *J. Phys. Chem. B* **105**, 11683-11701.
23
24
25 Zhang, R., Suh, I., Zhao, J., Zhang, D., Fortner, E. C., Tie, X., Molina, L. T., and Molina,
26 M. J. (2004), Atmospheric new particle formation enhanced by organic acids,
27 *Science* **304**, 1487-1490.
28
29
30 Zhang, R., Wang, L., Khalizov, A. F., Zhao, J., Zheng, J., McGraw, R., and Molina, L. T.
31 (2009), Formation of nanoparticles of blue haze enhanced by anthropogenic
32 pollution, *Proc. Natl. Acad. Sci.* **106**, 17650-17654.
33
34
35 Zhao, J., Khalizov, A., Zhang, R., and McGraw, R. (2009), Hydrogen-bonding interaction
36 in molecular complexes and clusters of aerosol nucleation precursors, *J. Phys.*
37 *Chem. A* **113**, 680-689.
38
39
40
41
42
43
44
45
46
47
48
49
50
51
52
53
54
55
56
57
58
59
60

| Property | <i>l</i> -menthol | <i>n</i> -nonane | <i>n</i> -butanol | water |
|-----------------------|------------------------|------------------------|------------------------|------------------------|
| S_{cr} | 111.5 | 7.41 | 3.11 | 3.20 |
| $T(K)$ | 323.15 | 300 | 300 | 298.15 |
| Ω/T | 4.19 | 2.40 | 1.64 | 1.69 |
| g^* | 23.6 | 57.8 | 101.6 | 102.2 |
| W_{homo}^*/kT | 55.5 | 57.9 | 57.7 | 59.5 |
| $n_v^{eq} (cm^{-3})$ | 1.19×10^{16} | 1.57×10^{17} | 2.58×10^{17} | 7.69×10^{17} |
| $f^{min} (N=1)$ | 0.230 | 0.244 | 0.254 | 0.251 |
| $h(f^{min})$ | 2.98 | 1.20 | 0.66 | 0.68 |
| n_{seed}^{min} | 5.4 | 14.1 | 25.8 | 25.7 |
| $v_1 (cm^3)$ | 2.38×10^{-22} | 2.99×10^{-22} | 1.53×10^{-22} | 3.00×10^{-23} |
| $d_{seed}^{min} (nm)$ | 1.35 | 2.00 | 1.96 | 1.14 |

Table 1. Parameters and scaling properties for the four working fluids included in Fig. 7 and the theoretical minimum particle size (d_{seed}^{min}) that can be detected by each for $N = 1 cm^{-3}$ at the threshold conditions $J_{homo} = J_{hetero} = 1$. Other properties include the critical saturation ratio for homogeneous nucleation, S_{cr} ; dimensionless corresponding states parameter, Ω/T ; log vapor saturation ratio in unstable equilibrium with the minimum detectable particle size, h ; molecular number concentration of vapor in equilibrium with bulk liquid, n_v^{eq} ; and the volume per molecule of bulk liquid working fluid, v_1 . Note comparative constancies of homogeneous nucleation barrier height and $f^{min} = n_{seed}^{min} / g^*$. Data sources: *l*-menthol, Becker and Reiss (1978); *n*-nonane, Rudek et al. (1996); *n*-butanol, Magnusson et al. (2003); water: Wölk and Strey (2001).

Figure Captions:

Figure 1. Area constructions derived from the Kelvin curve. Solid curve is the Kelvin curve for water from Equation 2.1. Horizontal dashed line is for a water vapor saturation ratio of 2 (relative humidity = 200%). The point of intersection marks the critical drop size, g^* consisting of the seed particle plus $n^* = g^* - v_{seed} / v_l$ molecules of condensed water. See text for interpretation of labeled areas $R_1 - R_4$ and tangent line.

Figure 2. Scaled nucleation barrier profiles from Equation 2.7 for several seed volume fractions ($f = n_{seed} / g^*$). Curves top to bottom: homogeneous nucleation case ($f = 0$), an intermediate heterogeneous nucleation case ($f = 0.25$), and the Kelvin limit ($f = 1$).

Figure 3. Typical behavior of the mean first passage time (MFPT) to reach a given cluster size as a function of that size. n is the number of molecules condensed onto the seed. Region I, quasi-equilibrium between clusters of pre-critical size. Region II, inflection point at the critical size. Region III, rapid growth regime. Calculations are for heterogeneous nucleation of *l*-menthol on a 1.5nm diameter seed. $S_{ext} = 86.0$, $W^* / kT = 18.1$, $J_1 = 1 s^{-1}$.

Figure 4. Nucleation rates for menthol. Solid curve is the Kelvin limit. Dashed lines and curves are contours of constant nucleation rate. Horizontal lines: contours of constant homogeneous nucleation rate for, top to bottom, $J_{homo} = 100, 1, \text{ and } 0.01 \text{ cm}^{-3} \text{ s}^{-1}$. Dashed curves give similar contours for the heterogeneous nucleation rate from the new

1
2
3 approximate prefactor-exponent form: top to bottom, $J_{hetero} = 100, 1, \text{ and } 0.01 \text{ cm}^{-3}\text{s}^{-1}$
4
5
6 for $N = 1 \text{ cm}^{-3}$. Markers: results from the double summation calculation for mean first
7
8 passage time and $J_1 = 1 \text{ cm}^{-3}\text{s}^{-1}$. These show excellent agreement with the approximate
9
10 result (middle curve).
11
12

13
14
15 Figure 5. Nucleation rates for water. Solid curve is the Kelvin limit. Dashed lines and
16
17 curves are contours of constant nucleation rate. Horizontal lines: contours of constant
18
19 homogeneous nucleation rate for, top to bottom, $J_{homo} = 100, 1, \text{ and } 0.01 \text{ cm}^{-3}\text{s}^{-1}$. Dashed
20
21 curves give similar contours for the heterogeneous nucleation rate from the new
22
23 approximate prefactor-exponent form: top to bottom, $J_{hetero} = 100, 1, \text{ and } 0.01 \text{ cm}^{-3}\text{s}^{-1}$
24
25 for $N = 1 \text{ cm}^{-3}$. Markers: results from the double summation calculation for mean first
26
27 passage time and $J_1 = 1 \text{ s}^{-1}$. These show excellent agreement with the approximate result
28
29 (middle curve).
30
31
32
33
34
35
36
37

38 Figure 6. Curves of equal heterogeneous and homogeneous nucleation rates ($SNR = 1$)
39
40 for *n*-butanol. Logarithm of $n_v^{eq}e^{-R_2}$ or N (these are equal along these curves from
41
42 **Equation 5.1**) versus seed diameter (nm). Solid curves: $T = 300\text{K}$, top to bottom
43
44 $J = 10^6$ ($S_{ext} = 3.67$), 1 ($S_{ext} = 3.11$), 10^{-6} ($S_{ext} = 2.78$). Dashed curves: $T = 320\text{K}$, top to
45
46 bottom $J = 10^6$ ($S_{ext} = 2.87$), 1 ($S_{ext} = 2.56$), 10^{-6} ($S_{ext} = 2.31$). Results are shown for
47
48 $d_{seed} / d_{Kelvin} < 0.8$ beyond which the barrier height is lower than $5kT$. Signal-to-noise
49
50 ratios for a given set of conditions exceed (are less than) unity to the right and above (left
51
52
53
54
55
56
57
58
59
60

and below) the corresponding curve. Horizontal lines: typical range for N in CPC measurements ($10^1 - 10^3 \text{ cm}^{-3}$).

Figure 7. Scaled nucleation rate. Dashed hyperbolic curves: contours of constant homogeneous nucleation barrier height, 50 kT (lower curve) and 70 kT (upper curve). The region between these curves provides a good indication of homogeneous nucleation threshold range for most substances. Markers show four candidate working fluids and are centered on critical cluster size and the critical saturation ratio (as indicated here for the case of nonane), which for each fluid gives $J_{\text{homo}} = 1$. Error bars show a four order of magnitude range in nucleation rate from $J_{\text{homo}} = 0.01$ to 100 . No error bar means that the height of the symbol itself exceeds this range. The solid curve is the Kelvin curve for nonane ($\Omega/T = 2.40$ at $T = 300 \text{ K}$). The horizontal and vertical dotted lines for nonane mark the logarithm of its critical saturation ratio $\ln(S_{\text{cr}})$ and g^* , respectively. The area of the rectangle bounded by these lines and the axes is twice the reduced barrier height, W_{homo}^* / kT . The caret marks the $N = 1 \text{ cm}^{-3}$ detection limit for nonane.

Figure 8. Area construction similar to Fig. 1 but illustrating the effect of interactions that lower the equilibrium vapor pressure relative to the Kelvin curve (solid curve). The dotted curve, which only departs from Kelvin at the smallest cluster sizes, results in a lowering of the barrier height for homogeneous nucleation to $R_1 + R_2 - \kappa$. The dashed curve shows lowering of the heterogeneous barrier from R_1 to $R_1 - \delta$. h is the length of the vertical line segment (see S18 of supplementary material). Note that the abscissa (upper scale) has been shifted in the heterogeneous case to tally only the number of

1
2
3
4
5
6
7
8
9
10
11
12
13
14
15
16
17
18
19
20
21
22
23
24
25
26
27
28
29
30
31
32
33
34
35
36
37
38
39
40
41
42
43
44
45
46
47
48
49
50
51
52
53
54
55
56
57
58
59
60

molecules of condensed working fluid. The lower scale, which runs out to g^* applies to the homogeneous case.

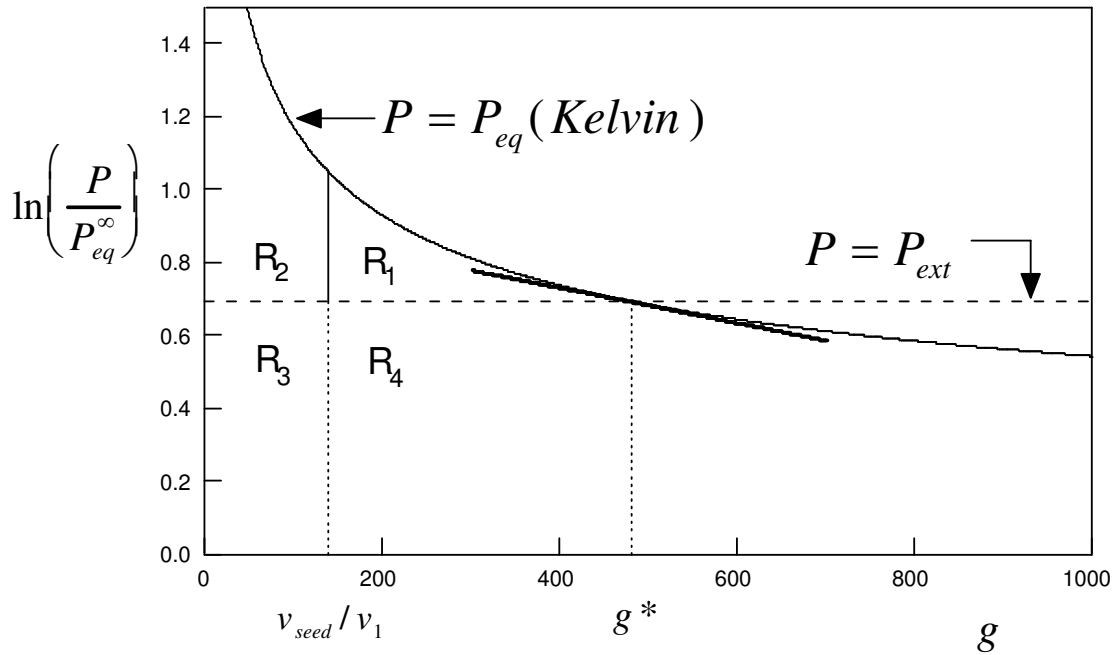


Figure 1

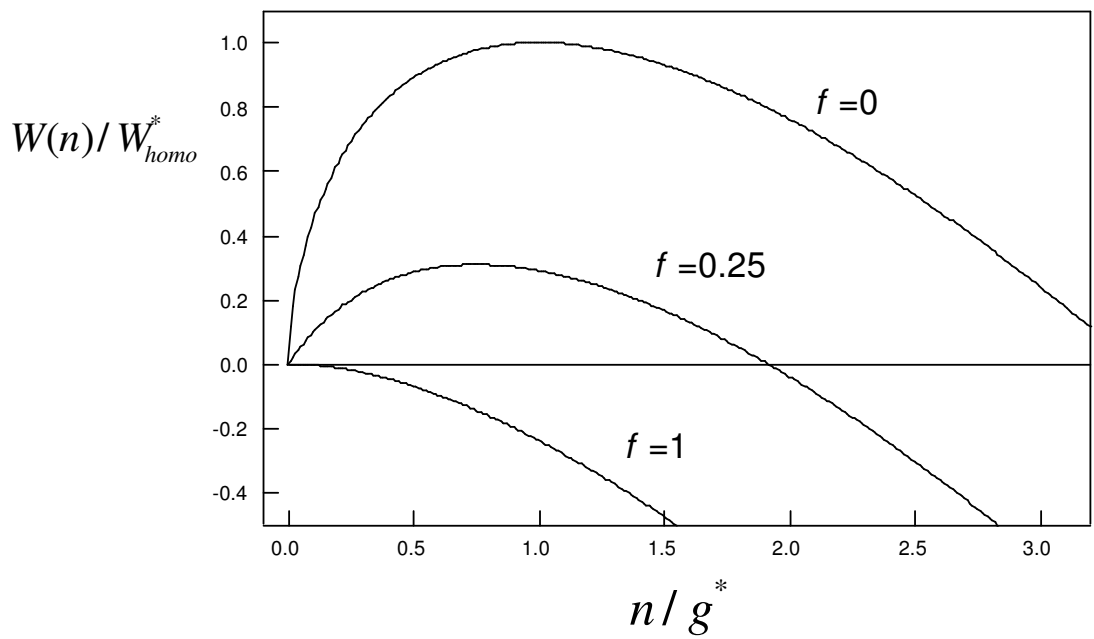


Figure 2

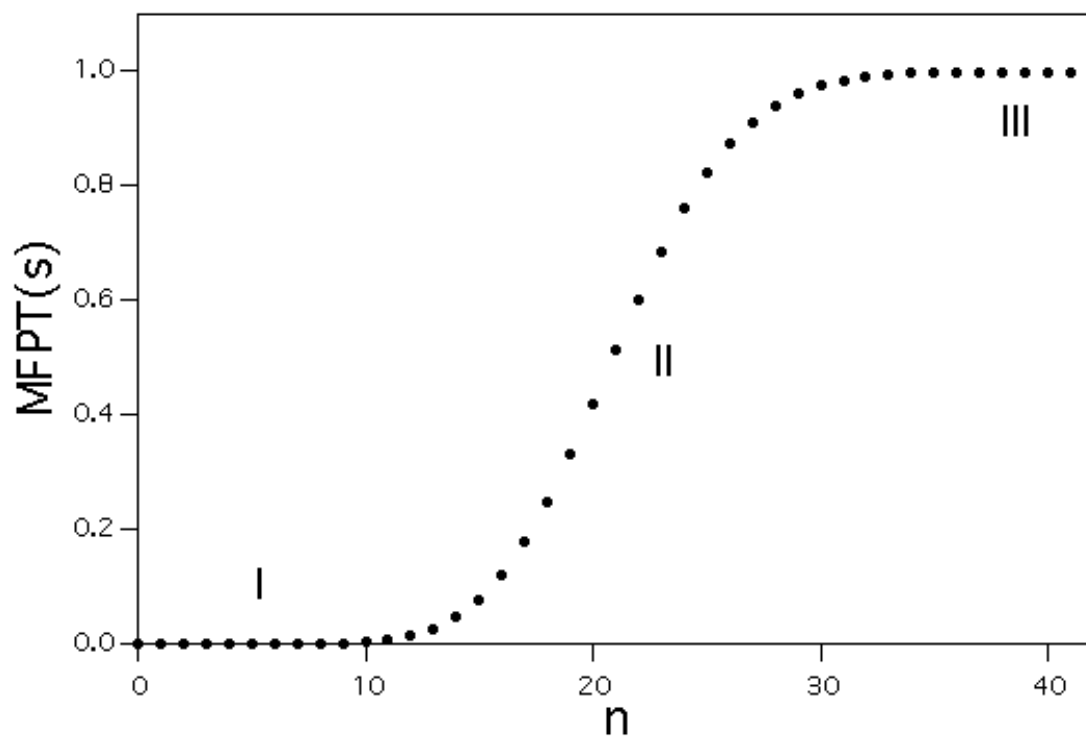


Figure 3

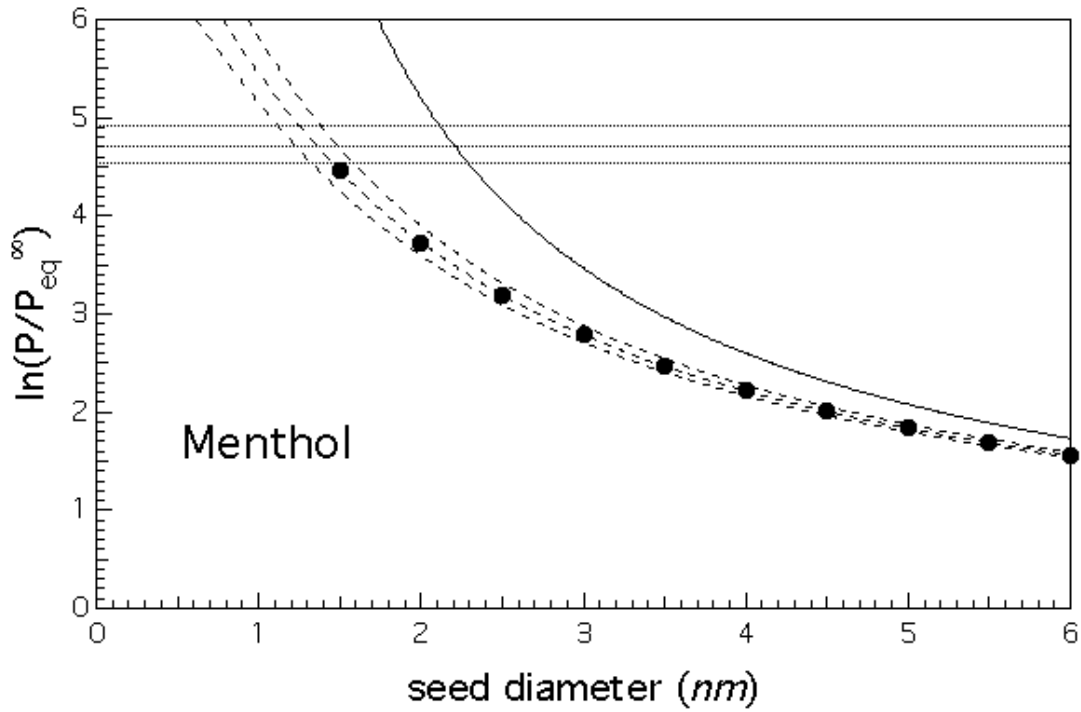


Figure 4

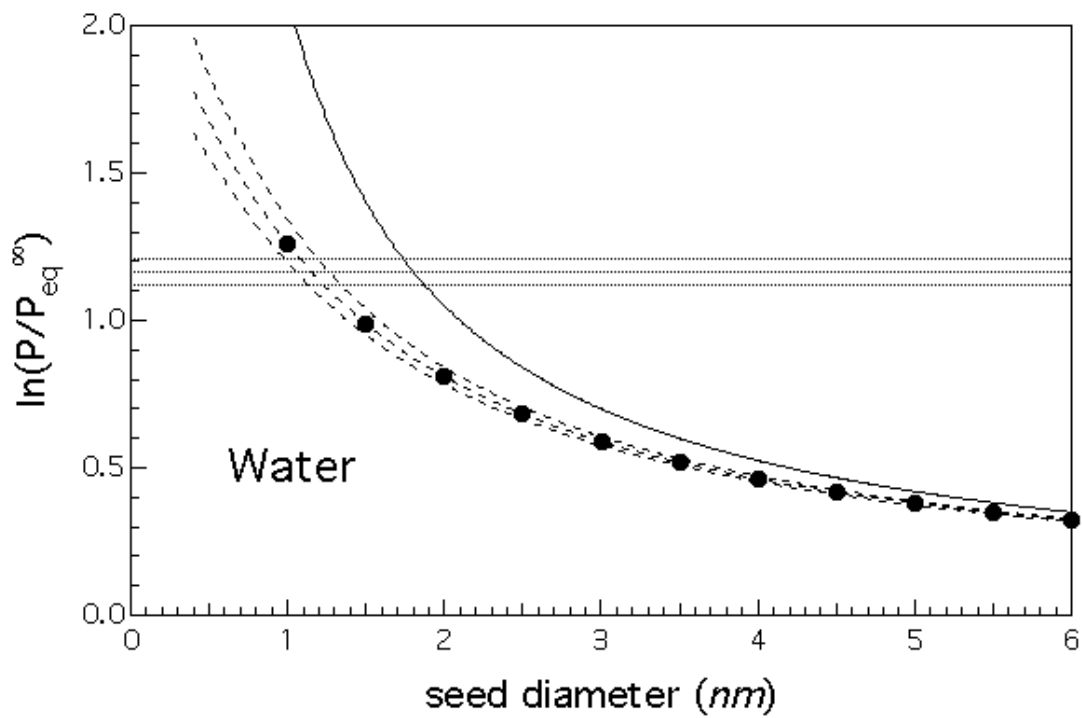


Figure 5

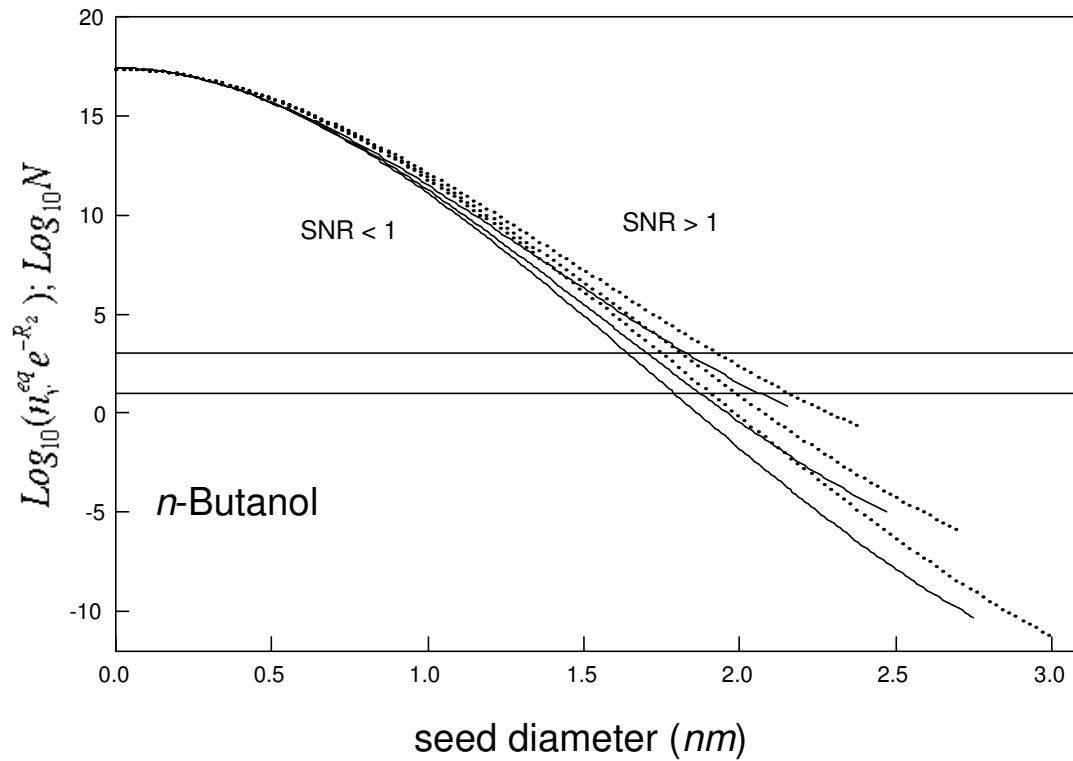


Figure 6

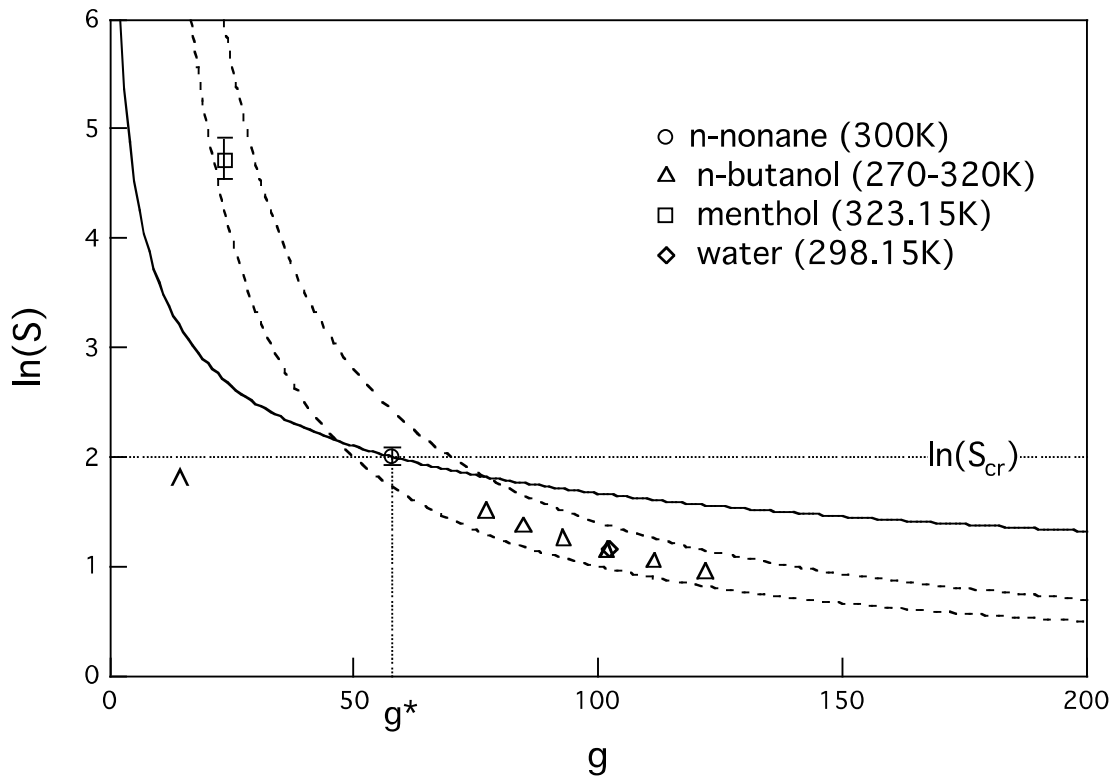


Figure 7

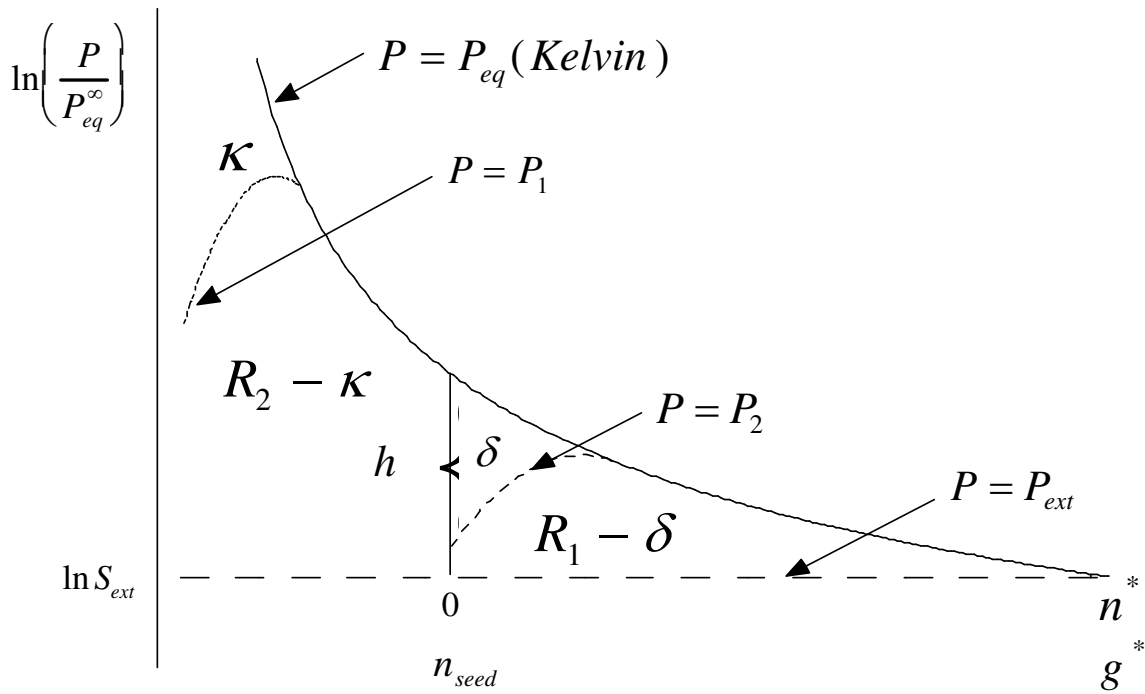


Figure 8

Supplemental Information

“Kinetics of heterogeneous nucleation in supersaturated vapor: Fundamental limits to neutral particle detection”

Robert McGraw, Jian Wang, and Chongai Kuang

(1) AREA CONSTRUCTIONS

1.1 From capillary theory: The first derivation uses the capillary theory and generates the areas with respect to the Kelvin curve (S1) as shown in Fig. 1.

$$P_{eq}(n) = P_{eq}^{\infty} \exp\left[-\frac{2\sigma v_1}{kTr(n)}\right] \quad (S1)$$

P_{eq}^{∞} is the equilibrium vapor pressure over a flat surface, σ is surface tension, v_1 is molecular volume in the bulk liquid phase, n is the number of molecules in the (homogeneous) drop, and $r(n) = [3nv_1/(4\pi)]^{1/3}$ is drop radius. The first integral to consider is the total area under the Kelvin curve out to a drop of size g :

$$\begin{aligned} I_1(g) &\equiv \int_0^g \ln \frac{P_{eq}(n)}{P_{eq}^{\infty}} dn = \int_0^g \frac{2\sigma v_1}{kTr(n)} dn = \left(\frac{32\pi}{3}\right)^{1/3} \frac{\sigma v_1^{2/3}}{kT} \int_0^g n^{-1/3} dn \\ &= (36\pi)^{1/3} \frac{\sigma v_1^{2/3}}{kT} g^{2/3} = \frac{A(g)\sigma}{kT} \end{aligned} \quad (S2)$$

where $A(g)$ is the surface area of the drop. At the critical size $I_1(g^*) = A(g^*)\sigma/kT = R_1 + R_2 + R_3 + R_4$, which is the total area under the curve shown in Fig. 1. For the second integral consider the area bounded above by the Kelvin curve and below by the line $\ln(P_{ext}/P_{eq}^{\infty})$, where P_{ext} is the external (supersaturated) vapor pressure:

$$I_2(g) \equiv \int_0^g \ln \frac{P_{eq}(n)}{P_{eq}^{\infty}} dn - \int_0^g \ln \frac{P_{ext}}{P_{eq}^{\infty}} dn = I_1(g) - g \ln \frac{P_{ext}}{P_{eq}^{\infty}} = I_1(g) - g \ln S_{ext}. \quad (S3)$$

where S_{ext} is the saturation ratio. Combining S2 and S3 shows that $I_2(g)$ is just the classical barrier profile in homogeneous nucleation theory:

$$I_2(g) = -g \ln S_{ext} + \frac{A(g)\sigma}{kT} = \frac{W_{homo}(g)}{kT} \quad (S4)$$

where $W_{homo}(g)$ is the reversible work of forming the g -mer drop from vapor at pressure

P_{ext} . At the critical drop size:

$$I_2(g^*) = W_{homo}^* / kT = R_1 + R_2, \quad (S5)$$

which is Eq. 2.3. Combining a result due to Gibbs [Gibbs 1906],

$W_{homo}^* = A(g^*)\sigma/3 = (R_1 + R_2 + R_3 + R_4)/3 = R_1 + R_2$, with S4, evaluated at g^* , gives Eqs

2.5a and 2.5b and the area proportion $R_3 + R_4 = 2(R_1 + R_2)$, all of which hold whenever

the droplet vapor pressure is given by the Kelvin relation.

Heterogeneous nucleation barriers are computed relative to the seed effective size

n_{seed} . Defining $n = g - n_{seed}$ gives Eq. 2.6:

$$\frac{W(n)}{kT} = I_2(g) - I_2(n_{seed}) = -n \ln S_{ext} + (36\pi)^{1/3} \left(\frac{\Omega}{T} \right) (g^{2/3} - n_{seed}^{2/3}) \quad (S6)$$

Note, with this definition of n , that the first equality is identical to Eq. 2.2. Evaluation at

the critical size gives $W(n^*)/kT = I_2(g^*) - I_2(n_{seed}) = R_1$, which is Eq. 2.4. For $n_{seed} = 0$,

these last results apply as well to the homogeneous nucleation case.

1.2 General results beyond the capillary theory: An alternative derivation that transcends

the Kelvin relation is achieved by applying detailed balance to the kinetics of particle

evaporation and growth. The approach, which requires only the law of mass action (ideal

vapor) and principle of detailed balance, is conceptually straightforward and suggests a

generality for Eq. 2.2 that extends well beyond the capillary theory. The derivation that

follows makes use of the kinetic potential [Wu, 1997] and is similar to that used in the

recent development of area constructions for deliquescence and efflorescence [McGraw

and Lewis, 2009], but tailored here specifically to homogeneous/heterogeneous vapor-to-liquid condensation.

Consider the exchange of vapor between clusters of size g and $g+1$. (The drop model is not required here as capillary theory isn't used). According to detailed balance:

$$\beta_g n_g^{eq} = \gamma_{g+1} n_{g+1}^{eq} \quad (S7)$$

where $\beta_g(\gamma_g)$ is the rate of vapor condensation (evaporation) and n_g^{eq} is the constrained equilibrium concentration for clusters of size g . The latter, satisfies the Boltzmann form:

$$n_g^{eq} \propto \exp\left[-\frac{W(g)}{kT}\right] \quad (S8)$$

where $W(g)$ is now the reversible work required to form a cluster of size g from the vapor. From S7 and S8:

$$\frac{W(g+1) - W(g)}{kT} = \ln\left(\frac{n_g^{eq}}{n_{g+1}^{eq}}\right) = \ln\left(\frac{\gamma_{g+1}}{\beta_g}\right). \quad (S9)$$

Adding such differences for a sequence of evaporation/condensation steps gives:

$$\begin{aligned} \frac{W(g_2) - W(g_1)}{kT} &= \ln\left(\frac{n_{g_1}^{eq}}{n_{g_2}^{eq}}\right) = \ln\left(\frac{n_{g_1}^{eq}}{n_{g_1+1}^{eq}} \frac{n_{g_1+1}^{eq}}{n_{g_1+2}^{eq}} \dots \frac{n_{g_2-1}^{eq}}{n_{g_2}^{eq}}\right) = -\ln\left(\frac{\beta_{g_1}}{\gamma_{g_1+1}} \frac{\beta_{g_1+1}}{\gamma_{g_1+2}} \dots \frac{\beta_{g_2-1}}{\gamma_{g_2}}\right) \\ &= -\sum_{g=g_1}^{g_2-1} \ln\left(\frac{\beta_g}{\gamma_{g+1}}\right). \end{aligned} \quad (S10)$$

The right hand side of S10 is a difference in kinetic potential [Wu, 1997]. For a single particle in equilibrium with its vapor the condensation rate β_g^{eq} equals the evaporation rate γ_{g+1} . This allows Eq. S10 to be rewritten using the identity:

$$\frac{\beta_g}{\gamma_{g+1}} = \frac{\beta_g}{\beta_g^{eq}} \frac{\beta_g^{eq}}{\gamma_{g+1}} = \frac{\beta_g}{\beta_g^{eq}} \quad (S11)$$

in the form

$$\frac{W(g_2) - W(g_1)}{kT} = - \sum_{g=g_1}^{g_2-1} \ln \left(\frac{\beta_g}{\beta_g^{eq}} \right) = - \sum_{g=g_1}^{g_2-1} \ln \left(\frac{P_{ext}}{P_1(g)} \right) = \sum_{g=g_1}^{g_2-1} \ln \left(\frac{P_1(g)}{P_{ext}} \right). \quad (S12)$$

where $P_1(g)$ is now the “true” g -cluster vapor pressure of Sec. 6. The last equalities of S12 make use of the proportionality between vapor condensation rate and vapor pressure for ideal vapors. S12 provides a basis for all of the area constructions given in the text: Approximating the right hand side as an integral, setting $P_1(g) = P_{eq}(g)$, where $P_{eq}(g)$ is given by the Kelvin relation, and the lower limit of integration to zero gives an alternative derivation of Eq. 2.2. The more general results of Sec. 6 (e.g. Eqs. 6.1 and 6.2) exceed the limits of capillary theory and require a more general approach, like S7-S12, that avoids artificial separation into surface and bulk properties inherent in the drop model.

(2) DERIVATION OF EQ. 4.7

Begin with Eq. 3.6:

$$\tau(nmax) = \sum_{j=0}^{nmax} \left(\frac{e^{W_{hetero}(j)/kT}}{D_j} \sum_{i=0}^j e^{-W_{hetero}(i)/kT} \right) \quad (S13)$$

and the typical behavior of $\tau(n)$ versus n shown in Fig. 3. In addition to separation along the time coordinate, discussed at the beginning of Sec. 4, there is a distinct separation with respect to particle size: The overwhelming majority of rapidly equilibrated pre-critical clusters tend to be significantly smaller than the critical particle size and dominate the summation over i . On the other hand the summation over j is dominated by terms near the critical size where the barrier is highest. Accordingly, to good approximation, the double summation factors into a product of two single-index summations. Specifically, the size separation allows one to choose a value, $imax$, such that terms in the inner summation having $i > imax$ may be neglected even though $imax$ is still significantly

smaller than the critical size. Meanwhile the critical size so dominates the summation over j that terms in the outer summation having $j \leq imax$ may be neglected. Modifying the ranges of the two indices to cover only non-neglected terms gives the expression to the right of the approximate equality, below, and the factorization:

$$\begin{aligned} \tau(2n^*) &= \frac{1}{J_1} \approx \sum_{j=imax+1}^{2n^*} \left(\frac{e^{W_{hetero}(j)/kT}}{D_j} \sum_{i=0}^{imax} e^{-W_{hetero}(i)/kT} \right) \\ &= \sum_{j=imax+1}^{2n^*} \frac{e^{W_{hetero}(j)/kT}}{D_j} \sum_{i=0}^{imax} e^{-W_{hetero}(i)/kT} \end{aligned} \quad (S14)$$

where, as described in Sec. 4, we have set $nmax = 2n^*$. A series of further approximations is now made to the factored expression: First D_j is approximated by its value at the critical size

$$D_j \approx D_{j^*} = n_v \sqrt{\frac{8\pi kT}{m_v}} r_1^2 (n_{seed} + j^*)^{2/3} = \frac{P_{ext} A(j^*)}{\sqrt{2\pi m_v kT}} \quad (S15)$$

and factored out of the summation. Second, the remaining part of the summation over j is approximated in the usual manner of nucleation theory by its maximum term multiplied by the Zeldovich factor to yield the intermediate result:

$$\tau(2n^*) = \frac{1}{J_1} \approx \frac{1}{D_{j^*}} \frac{1}{Z} e^{W_{hetero}(j^*)/kT} \sum_{i=0}^{imax} e^{-W_{hetero}(i)/kT} \quad (S16)$$

The i^{th} term of the last summation is a Boltzmann factor proportional to the quasi-equilibrium number concentration of seed-condensate particles of size $n = i$. Thus the total number concentration of pre-critical particles is proportional to the summation itself.

Linearization of the reduced work about $i = 0$ gives

$$W_{hetero}(i)/kT \equiv R_1(i) \approx hi \quad (S17)$$

where $R_1(i)$ is the partial area of region 1 of Fig. 1 from $n = 0$ to $n = i$. S17 follows from the fact that $R_1(0) = 0$ and $(dR_1/di)_{i=0} = h$. Geometrically, h is the length of the solid vertical line segment separating regions R_1 and R_2 in Fig. 1 and is readily evaluated for the Kelvin curve:

$$\begin{aligned} h &\equiv \ln\left(\frac{P_{eq}}{P_{eq}^\infty}\right) - \ln\left(\frac{P_{ext}}{P_{eq}^\infty}\right) = \left(\frac{32\pi}{3}\right)^{1/3} \frac{\Omega}{T} [(n_{seed})^{-1/3} - (g^*)^{-1/3}] \\ &= \left(\frac{32\pi}{3}\right)^{1/3} \frac{\Omega}{T} (g^*)^{-1/3} (f^{-1/3} - 1) = \ln\left(\frac{P_{ext}}{P_{eq}^\infty}\right) (f^{-1/3} - 1) = \ln S_{ext} (f^{-1/3} - 1) \end{aligned} \quad (S18)$$

The second and fourth equalities derive from Eq. 2.1 and the third from $n_{seed} = fg^*$. Apart from a dimensionless scaling factor $W_{homo}^*/g^*kT = \ln S_{ext}/2$ (Eq. 2.5a), h is the initial slope of the scaled, f -dependent barrier height shown in Fig. 2. This slope ranges from a very large value in the homogeneous nucleation limit ($n_{seed} = 0$; $n = 1$) to zero at the critical size. Under the assumed condition that a suitable $imax$ can be chosen such that the quasi-equilibrium number concentration of particles beyond MF_{imax} is a negligible fraction of the initial seed concentration, the summation appearing on the right hand side of S16 can be further approximated as:

$$\sum_{i=0}^{imax} e^{-W_{hetero}(i)/kT} \approx \sum_{i=0}^{imax} e^{-hi} \approx \sum_{i=0}^{\infty} e^{-hi} = \frac{1}{1 - e^{-h}} \quad (S19)$$

where in the first approximate equality S17 has been used. Substitution into S16 gives our final form (Eq. 4.1) for the per-seed heterogeneous nucleation rate (units s^{-1}):

$$J_1 = \frac{1}{\tau} \approx \frac{P_{ext} A(j^*)}{\sqrt{2\pi m_v kT}} (1 - e^{-h}) Z e^{-W_{hetero}^*/kT} \quad (S20)$$

References:

Gibbs, J. W. (1906). The Scientific Papers of J. Willard Gibbs (Longmans, Green, and Co., London) Vol. 1, pg. 258.

1
2
3
4
5 Wu, D. T. (1997). Nucleation theory, Solid State Physics **50**, 37-187.
6
7
8
9
10
11
12
13
14
15
16
17
18
19
20
21
22
23
24
25
26
27
28
29
30
31
32
33
34
35
36
37
38
39
40
41
42
43
44
45
46
47
48
49
50
51
52
53
54
55
56
57
58
59
60